

# Gravito-inertial and pressure modes detected in the B3 IV CoRoT target HD 43317<sup>★,★★,★★★</sup>

P. I. Pápics<sup>1</sup>, M. Briquet<sup>2,★★★</sup>, A. Baglin<sup>3</sup>, E. Poretti<sup>4</sup>, C. Aerts<sup>1,5</sup>, P. Degroote<sup>1</sup>, A. Tkachenko<sup>1</sup>, T. Morel<sup>2</sup>, W. Zima<sup>1</sup>, E. Niemczura<sup>6</sup>, M. Rainer<sup>4</sup>, M. Hareter<sup>7</sup>, F. Baudin<sup>8</sup>, C. Catala<sup>9</sup>, E. Michel<sup>9</sup>, R. Samadi<sup>9</sup>, and M. Auvergne<sup>9</sup>

<sup>1</sup> Instituut voor Sterrenkunde, K.U.Leuven, Celestijnenlaan 200D, 3001 Leuven, Belgium  
e-mail: Peter.Papics@ster.kuleuven.be

<sup>2</sup> Institut d'Astrophysique et de Géophysique, Université de Liège, Allée du 6 Août 17, Bât. B5c, 4000 Liège, Belgium

<sup>3</sup> Laboratoire AIM, CEA/DSM-CNRS-Université Paris Diderot, CEA, IRFU, SAp, centre de Saclay, 91191 Gif-sur-Yvette, France

<sup>4</sup> INAF – Osservatorio Astronomico di Brera, via E. Bianchi 46, 23807 Merate (LC), Italy

<sup>5</sup> Department of Astrophysics, IMAPP, University of Nijmegen, PO Box 9010, 6500 GL Nijmegen, The Netherlands

<sup>6</sup> Instytut Astronomiczny, Uniwersytet Wrocławski, Kopernika 11, 51-622 Wrocław, Poland

<sup>7</sup> Institut für Astronomie, Universität Wien, Türkenschanzstrasse 17, 1180 Vienna, Austria

<sup>8</sup> Institut d'Astrophysique Spatiale, CNRS/Univ. Paris-Sud, Bât. 121, 91405 Orsay Cedex, France

<sup>9</sup> LESIA, UMR8109, Université Pierre et Marie Curie, Université Denis Diderot, Observatoire de Paris, 92195 Meudon Cedex, France

Received 11 January 2012 / Accepted 21 March 2012

## ABSTRACT

**Context.** OB stars are important building blocks of the Universe, but we have only a limited sample of them well understood enough from an asteroseismological point of view to provide feedback on the current evolutionary models. Our study adds one special case to this sample, with more observational constraints than for most of these stars.

**Aims.** Our goal is to analyse and interpret the pulsational behaviour of the B3 IV star HD 43317 using the CoRoT light curve along with the ground-based spectroscopy gathered by the HARPS instrument. This way we continue our efforts to map the  $\beta$  Cep and SPB instability strips.

**Methods.** We used different techniques to reveal the abundances and fundamental stellar parameters from the newly-obtained high-resolution spectra. We used various time-series analysis tools to explore the nature of variations present in the light curve. We calculated the moments and used the pixel-by-pixel method to look for line profile variations in the high-resolution spectra.

**Results.** We find that HD 43317 is a single fast rotator ( $v_{\text{rot}} \approx 50\% v_{\text{crit}}$ ) and hybrid SPB/ $\beta$  Cep-type pulsator with Solar metal abundances. We interpret the variations in photometry and spectroscopy as a result of rotational modulation connected to surface inhomogeneities, combined with the presence of both  $g$  and  $p$  mode pulsations. We detect a series of ten consecutive frequencies with an almost constant period spacing of 6339 s as well as a second shorter sequence consisting of seven frequencies with a spacing of 6380 s. The dominant frequencies fall in the regime of gravito-inertial modes.

**Key words.** asteroseismology – stars: variables: general – stars: abundances – stars: oscillations – stars: individual: HD 43317 – stars: rotation

## 1. Introduction

Asteroseismology is a tool which can be regarded as an *astrophysical stethoscope*. The detection and analysis of the effects of sound waves propagating through stellar interiors is one of the few ways in which we can deduce information about the insides of stars. We use light and radial velocity variations from pulsating stars along with theoretical models – continuously refined by the observations – to deduce information from below their surface. With the launch of space-based instruments such as the

CoRoT (Convection Rotation and planetary Transits, Auvergne et al. 2009) and *Kepler* (Gilliland et al. 2010) satellites, the availability of virtually uninterrupted photometric data sets at micro-magnitude precision has enabled us to sharpen our view, and opened up a new era in asteroseismology.

In this paper we are concerned with massive stars which are important building blocks in the chemistry of our Universe, enriching the interstellar matter – when they end their lives in a supernova explosion – with heavy elements they produced during their lifetimes. From an asteroseismic point of view, they are relatively easy to interpret. Stellar lifetime is strongly influenced by several internal mixing processes, such as those due to core overshooting and rotation, which are the major uncertainties in the present-day models. With the precision of data delivered by currently available space instruments, we aim to deduce a quantitative seismic estimate of the overshooting and internal rotation in B stars to calibrate stellar evolution models in the upper part of the Hertzsprung-Russel diagram (HRD) from a carefully selected sample of suitable pulsators.

\* The CoRoT space mission was developed and is operated by the French space agency CNES, with participation of ESA's RSSD and Science Programmes, Austria, Belgium, Brazil, Germany, and Spain.

\*\* Based on data gathered with HARPS installed on the 3.6 m ESO telescope (ESO Large Programme 182.D-0356) at La Silla, Chile.

\*\*\* Table A.1 is only available at the CDS via anonymous ftp to [cdsarc.u-strasbg.fr](http://cdsarc.u-strasbg.fr) (130.79.128.5) or via <http://cdsarc.u-strasbg.fr/viz-bin/qcat?J/A+A/542/A55>

\*\*\*\* F.R.S.-FNRS Postdoctoral Researcher, Belgium.

Slowly rotating pulsating OB stars situated in the upper part of the HRD have a relatively simple frequency content. In general, the more massive and hot  $\beta$  Cep stars oscillate in low-order  $p$  (and  $g$ ) modes with typical periods between about 3 and 8 h, while the less massive and cooler Slowly Pulsating B (SPB) stars oscillate in high-order  $g$  modes with periods between 0.8 and 3 days (Aerts et al. 2010). This simple picture gets more complicated by considering, for example, the presence of rotation. On the other hand, slow rotation can help mode identification by detecting multiplets of different modes. Given that these penetrate to different depths in the star, rotationally split multiplets offer the potential to infer the internal rotational profile (e.g., Kawaler et al. 1999; Aerts et al. 2003).

Based on CoRoT data seismic inferences on the interior structure of slowly rotating pulsating OB stars has been derived. While the power of present-day state-of-the-art modelling has been demonstrated for the B1.5 II-III  $\beta$  Cep star HD 180642 (Aerts et al. 2011), unexpected stochastic modes with constant frequency spacings were detected in the O8.5 V star HD 46149 (Degroote et al. 2010b). On the other hand, heat-driven  $\beta$  Cep-like modes were detected but not predicted to be excited in the O9 V star HD 46202 (Briquet et al. 2011) and vice-versa in the B0.5 IV star HD 51756 (Pápics et al. 2011). Degroote et al. (2010a) discovered an almost constant period spacing of the high-order  $g$  modes in the frequency spectrum of the B3 V hybrid SPB/ $\beta$  Cep star HD 50230, serving as a viable diagnostic to deduce the overshooting parameter for B pulsators. Moreover, the small periodic deviations from this spacing were used to model the diffusive mixing process around the core.

The B3 IV star HD 43317 was selected as our target in this context, as part of our attempts to increase the number of well-studied B stars. We were especially looking for a star with nearly identical parameters as those of HD 50230, but brighter, to see if it has similar behaviour of its  $g$  modes and to deduce the implications of a higher rotation velocity. In parallel with the monitoring done by CoRoT's asteroseismology CCD, we gathered ground-based spectroscopy to give as many observational constraints as possible, thus providing the foundations for stellar modelling.

## 2. Fundamental parameters

### 2.1. Prior to our study

HD 43317 is a bright field-star in the constellation of Orion. It was first mentioned in proper motion studies (e.g., Morgan 1956) and survey catalogues of early-type stars (e.g., Bonneau 1967). Further investigations include interstellar absorption and extinction measurements (Weber et al. 1971; Savage et al. 1985) and Galactic kinematic studies (e.g., Westin 1985), which are all common for B type stars. This is the first time that HD 43317 is investigated from an asteroseismic point of view.

There is good agreement on both the spectral type and luminosity class: B3 IV (Lesh 1968), B2 V (Guetter 1968), and B3 IV/V (Houk & Swift 1999). These classifications are all based on visual comparison of objective-prism plates to standard stars from a spectral atlas. There is one classification of B2.5 V using ultraviolet line features of S2/68 spectra (Cucchiari et al. 1976). Effective temperature estimates (based on the spectral type and different calibration tables) of 17 100 K and 17 900 K are given by Wright et al. (2003) and Hohle et al. (2010). Hohle et al. also give an estimated mass of  $6.05 \pm 0.69 M_{\odot}$ . Due to lack of high-quality spectroscopy, Lefever et al. (2010) could not include this star in their large sample of B stars in the CoRoT

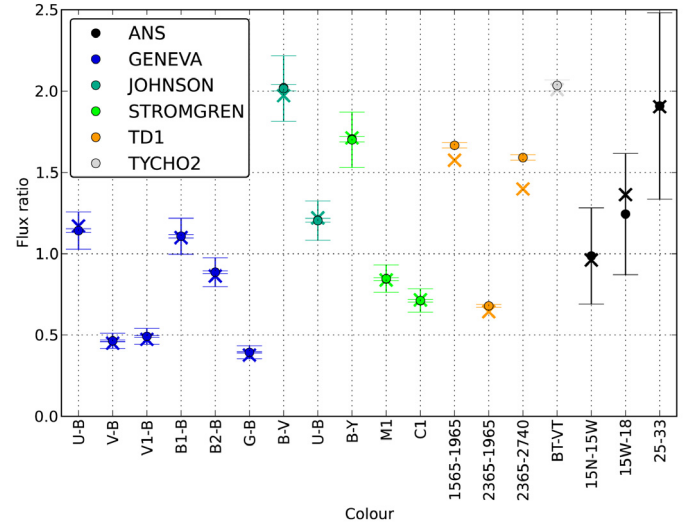


**Fig. 1.** Fitted flux ratios. Different marker colours denote different photometric systems, filter names are given on the x-axis. “X” symbols are synthetic (model) colours, circles are observed ones.

field-of-view to deduce the fundamental parameters and abundances with better precision.

Quoted estimates of the projected rotational velocity  $v \sin i$  are  $110 \pm 10 \text{ km s}^{-1}$  (Wolff et al. 1982) and  $130 \pm 16 \text{ km s}^{-1}$  (Abt et al. 2002). Distance measurements of  $369^{+73}_{-53} \text{ pc}$  (from a parallax of  $2.71 \pm 0.45 \text{ mas}$ , van Leeuwen 2007), 640 pc (Savage et al. 1985), 446 pc (Shull & van Steenberg 1985), and 598 pc (Heiles 2000) are available from different methods. Photometry led to  $V_{\text{mag}} = 6.64$ ,  $(B - V) = -0.17$ ,  $(U - B) = -0.66$ , and  $H_{\beta} = 2.665$  (Crawford et al. 1971); the data available for many more filters will be used in Sect. 2.2. Colour excess estimates of  $E(B - V)$  are between 0.03 (Savage et al. 1985) and 0.10 (Heiles 2000). From these values we derived an absolute magnitude estimate of  $M_V = -1.80 \pm 0.91$  which is consistent with the spectral type and luminosity class of the star (based on the tables provided by Straižys & Kurliene 1981).

### 2.2. SED-fitting

In an attempt to give better estimates of the fundamental parameters of HD 43317, the parameters were determined from multicolour photometry following the method described in Degroote et al. (2012). We used UV (ANS, TD1, Wesselius et al. 1982, 1980; Thompson et al. 1978), optical (Geneva, Johnson, Hipparcos, Tycho, Stromgren, Rufener 1988; Rufener & Nicolet 1988; Mermilliod 1986; Høg et al. 2000; Hauck & Mermilliod 1998), and near-infrared (2MASS, Wise, Cutri et al. 2003, 2011; Wright et al. 2010) photometry. No infrared excess was detected up to  $20 \mu\text{m}$  in the Akari (Murakami et al. 2007) and Wise bands. The photometry was fitted to LTE (Castelli & Kurucz 2003) and non-LTE (Lanz & Hubeny 2007) model atmospheres, using a method similar to the infrared-flux method by Blackwell et al. (1979), i.e., by using absolute calibrated values in the infrared and colours at shorter wavelengths. The best fit using the NLTE TLUSTY models (Lanz & Hubeny 2007) is shown in Fig. 1, while the results are listed in Table 1.

We will use recently obtained high-resolution spectra to derive the fundamental parameters along with the abundances in Sect. 4. This will be especially useful for the surface gravity value, as the photometric method is fairly insensitive to it, which is the reason why the best fit values are larger than the typical

**Table 1.** Stellar parameters derived from multicolour photometry using different model atmospheres.

Model	Kurucz	TLUSTY
$T_{\text{eff}}$ (K)	$17\,200^{+900}_{-700}$	$17\,350^{+950}_{-650}$
$\log g$ (cgs)	$4.75^{+0.25}_{-1.15}$	$4.75^{+0.00}_{-0.75}$
$\log Z/Z_{\odot}$	$-2^{+1}_{-0.5}$	$-0.8^{+0.5}_{-0.2}$
$E(B - V)$ (mag)	$0^{+0.02}_{-0.00}$	$0^{+0.03}_{-0.00}$
$\theta$ (mas)	$0.095^{+0.003}_{-0.003}$	$0.095^{+0.002}_{-0.003}$

**Notes.** Error ranges are set around the best fit value corresponding to the 90% confidence interval based on the  $\chi^2$  values.  $Z_{\odot} = 0.02$  dex.

ZAMS value of  $\sim 4.5$ , and for the metallicity, which is also poorly constrained from photometry.

### 3. The CoRoT light curve

#### 3.1. Frequency analysis

HD 43317 was observed by the CoRoT satellite as a primary target during the LRA03 long run of the mission as part of the asteroseismology programme, while monitoring a field in the direction of the anticentre of the Milky Way from HJD 2455 106.410969 for 150.41 days (covering five months from 1 October 2009 to 1 March 2010). All flagged observations were removed from the light curve, leaving us with 359 704 measurements (resulting in a duty cycle of almost 90%). It is necessary to delete the flagged CoRoT data points because of the passage of the satellite through the South Atlantic anomaly and some other low Earth orbit perturbations (see [Auvergne et al. 2009](#)). This introduces small gaps in the light curve in phase with the orbital period, which produces a spectral window with aliases at the orbital frequency (6184 s,  $13.97 \text{ d}^{-1}$ ,  $161.7 \mu\text{Hz}$ ) and its harmonics, at the frequency related to day/night variations ( $2 \text{ d}^{-1}$ ,  $23.15 \mu\text{Hz}$ ), and combinations of them. The most prominent aliases appear at frequencies  $f_j \pm n \times 13.97 \pm 1 \pm 2 \text{ d}^{-1}$ , where  $f_j$  is an intrinsic frequency, and  $n \in \mathbb{N}^*$  (see, e.g., [Gutiérrez-Soto et al. 2009](#)). These aliases are removed during the prewhitening process. We looked for trends which have a well known instrumental origin ([Auvergne et al. 2009](#)), and modelled them with various prescriptions. In order to correct the light curve for these instrumental effects, we divided it by a fitted linear polynomial. As after this initial step, there were no clear jumps or trends visible anymore, we used the resulting dataset (see Fig. 2) in our analysis.

##### 3.1.1. Common approach

The way one defines significance affects the final number of accepted frequencies in a Fourier-analysis. In the commonly used approach of [Breger et al. \(1993\)](#), one measures the signal-to-noise (S/N) level as the ratio of a given peak to the average residual noise in a given window around the peak or in a peak-free region, before (or after) prewhitening. This approach worked fine for ground-based photometry, with relatively few significant peaks in the data sets. With space-based instruments like CoRoT and *Kepler* delivering almost uninterrupted data with a precision typically two orders of magnitude better than ground-based photometry, forests of peaks emerge above the noise, and using the classical criteria is no longer obvious.

A simple model which uses a limited number of sine functions to describe the pulsations of a star is a good approach when

it comes to tens of frequencies, but when hundreds or even thousands of them occur, each leading to low variance reduction (see, e.g., [Poretti et al. 2009](#); [Chapellier et al. 2011](#)), we prefer a more conservative approach and accept less but more secure frequencies. Should any irregularities or previously undetected features arise thanks to the higher precision, we must be able to detect them without going down to the noise level.

We first performed an iterative prewhitening procedure whose description is already given by [Degroote et al. \(2009\)](#) and thus omitted here. This resulted in a list of amplitudes ( $A_j$ ), frequencies ( $f_j$ ), and phases ( $\theta_j$ ), by which the light curve can be modelled via  $n_f$  frequencies in the well-known form of

$$F(t_i) = c + \sum_{j=1}^{n_f} A_j \sin[2\pi(f_j t_i + \theta_j)].$$

The prewhitening procedure was stopped after removing 1353 frequencies (adopting a  $p$  value of  $p = 0.001$  in hypothesis testing). Unlike in the case of the  $\delta$  Scuti star HD 50844 ([Poretti et al. 2009](#)), the frequencies do not form a plateau below a given cutoff frequency.

Following the commonly used approach, we considered a frequency as significant if its amplitude exceeds a S/N ratio of 4 (see [Breger et al. 1993](#)), while the noise level is calculated as the average amplitude – before prewhitening – in a given interval centred on the frequency of interest. We checked the effect of changing the width of the window in which we measure the noise levels between the prewhitening steps. Setting the window width at  $1 \text{ d}^{-1}$  or  $3 \text{ d}^{-1}$  resulted in 107 or 149 frequencies having a S/N level higher than 4 (confidence level 99.9% in the case of white Gaussian noise), respectively. For comparison, a window width over the entire considered frequency range of  $20 \text{ d}^{-1}$  would result in 394 frequencies with a S/N above 4. Changing the significance criterion from 4 to 3.6 or 3 times the residual amplitude before prewhitening – corresponding to 95% or 80% confidence levels ([Kuschnig et al. 1997](#)) – raises the number of significant frequencies from 107–149–394 to 145–186–498 and 297–375–765, respectively. We continued with the 4 S/N criterion.

Raising the number of frequencies in the model from 107 to 394 lowers the residual noise levels (calculated in  $3 \text{ d}^{-1}$  wide windows centred around 1.5, 5 and  $10 \text{ d}^{-1}$ ) from 10.4–3.7–1.3 ppm to 1.9–1.8–1.2 ppm (compared to the average signal levels of 92.4–26.9–4.6 in the original data). Subtracting a model using 107, 149 or 394 frequencies results in a variance reduction of 96.27%, 97.73%, and 98.93%, respectively.

To compare different models, constructed using different sets of parameters, calculation of statistics is useful, like Akaike’s Information Criterion (AIC) and the Bayesian Information Criterion (BIC) (see, e.g., [Degroote et al. 2009](#); [Blomme et al. 2011](#)). The AIC is defined as

$$\text{AIC} = 2k - 2 \ln \mathcal{L}_{\text{max}} \approx n \ln(\text{RSS}/n) + 2k + n,$$

where  $\mathcal{L}_{\text{max}}$  is a maximum likelihood estimator (MLE),  $n$  is the effective number of observations, and  $k$  is the number of free parameters in the model. Under the assumption of Gaussian white noise, we can insert the MLE of the noise variance,  $\sigma_i^2 = \text{RSS}/n$  with RSS being the residual sum of squares. The BIC is defined as

$$\text{BIC} = -2 \ln \mathcal{L}_{\text{max}} + k \ln n \approx n \ln(\text{RSS}/n) + k \ln n.$$

Both the AIC and the BIC are only relevant in comparisons; the lower their values, the better the model. Unlike the variance reduction, they discourage the use of many free parameters. As

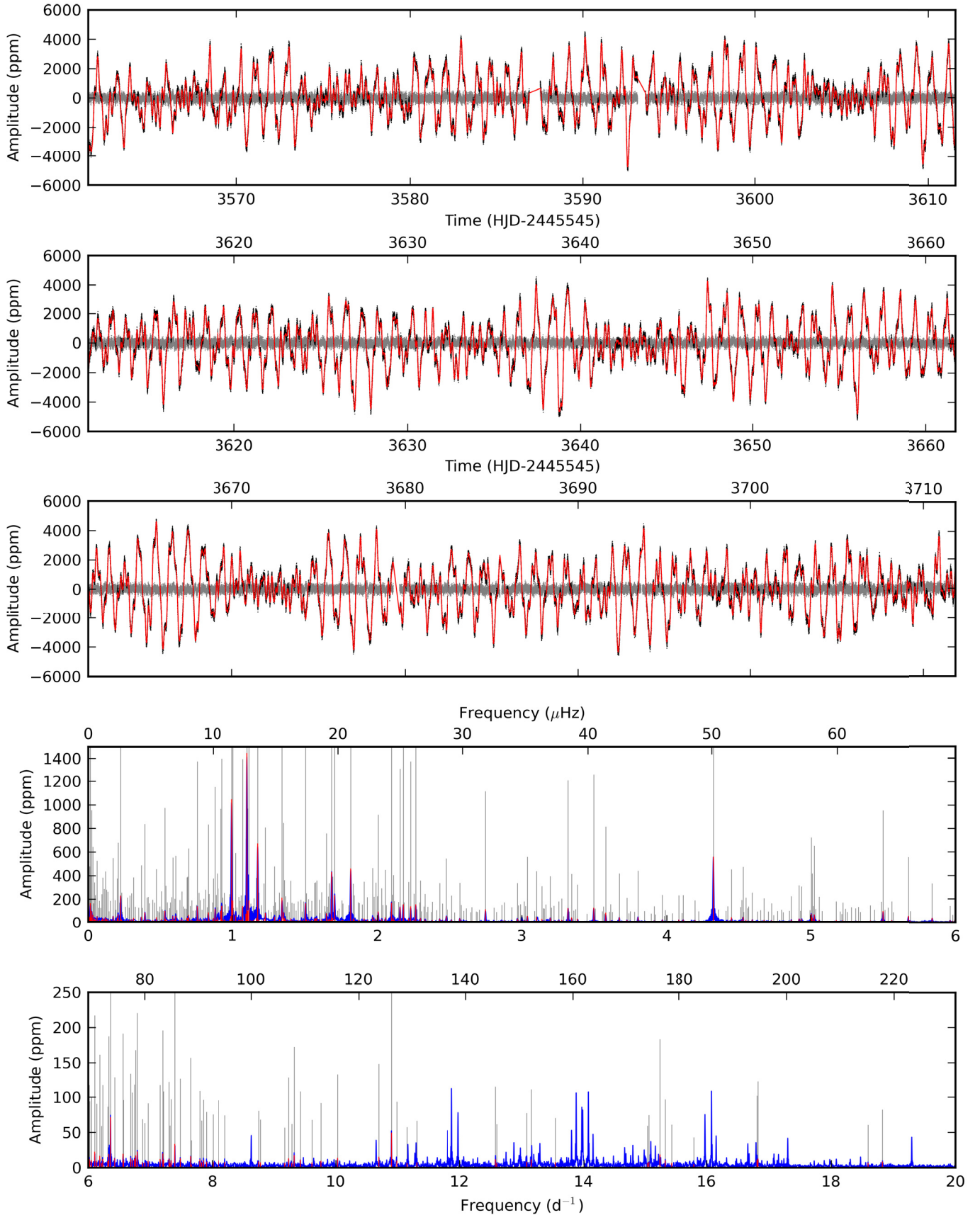


**Fig. 2.** *Upper three panels:* the reduced CoRoT light curve (black dots, brightest at the top) and residuals (grey dots) after prewhitening with a model (red solid line) constructed using the set of 424 frequencies listed in Table A.1 – see text for further explanation. *Lower two panels:* the Scargle periodogram of the full CoRoT light curve (blue solid line) showing the 424 frequencies (red vertical lines). For better visibility, the red lines are repeated in grey in the background, after multiplying their amplitude with a factor ten. Aliases of the strongest peaks around  $\sim 1 \text{ d}^{-1}$  due to the satellite orbital motion can be seen around 12, 14 and  $16 \text{ d}^{-1}$ .

shown by Degroote et al. (2009), the BIC is more suitable when one wants to stress the importance of simpler models over more complicated ones as it increases the penalty for introducing new parameters. Although both the AIC or BIC values suggest that raising the number of free parameters in the model is useful from a viewpoint of these statistical criteria, it seems meaningless to understand the physics of the star, as raising to 800 frequencies in the fit only results in an additional 0.26% of variance reduction.

### 3.1.2. Alternative approach

It is clear that changes in the definitions of the used significance criteria strongly affect the number of accepted frequencies. To come to a final list of frequencies for interpretation, we divided the data set in two equally long time strings and ran the same iterative prewhitening procedure. The hypothesis testing for a  $p$  value of  $p = 0.001$  stopped the process at 736 and 760 frequencies for the first and second half. We compared the frequency content of the two parts of the data to each other and to the one of the full data set, following the matching frequency method described by Chapellier et al. (2011). We set the threshold of having equal frequencies to the Rayleigh limit of the full data set  $1/T = 0.00665 \text{ d}^{-1}$  and we required that amplitudes found in the subsets do not differ more than 50% from the amplitude which was found in the complete data set. Moreover, we also required that the  $n$ th prewhitened frequency in the subsets had to be among the first  $n \pm (10 \sqrt{n})$ th frequencies from the full data set to ensure that the order of prewhitening in the subsets does not differ too much from the one in the full set. In this way we found 217 frequencies common for both halves and the full data set.

A model constructed using these 217 frequencies gives a variance reduction of 96.30%. To correct for the loss of the lowest frequencies, we completed the set of common frequencies with those peaks which only appear in the full data set at  $S/N > 4$ . This gives an additional 16, 35, or 207 frequencies when a window width of  $1 \text{ d}^{-1}$ ,  $3 \text{ d}^{-1}$ , or  $20 \text{ d}^{-1}$  is used to calculate the noise levels. Using these additional frequencies to construct a model with 233, 252 or 424 frequencies leads to clearly better fits with a variance reduction of 97.58%, 98.11%, or 98.95%.

Looking at the residual light curves, our approach is more solid than simply using the classical S/N criterion on the full data set. Thus, we accept the set of 424 frequencies (listed in Table A.1) as the final model of the light curve. The orbital frequency of the CoRoT satellite was weakly detected, but it did not fit the selection criteria. The aliases – some of which can be easily seen in Fig. 2 – introduced by the orbit of the CoRoT satellite were removed by the iterative prewhitening procedure. The noise level in the periodogram calculated from the residuals around  $1.5\text{--}5\text{--}10 \text{ d}^{-1}$  is  $2.0\text{--}1.8\text{--}1.1$  ppm, respectively. To be conservative and to avoid being completely overwhelmed by the large number of low-amplitude frequencies due to the large window width for the S/N computation, we use the secure set of 252 frequencies when we look for characteristic mode frequency spacings in Sect. 5 in order to focus future modelling on those first. We do point out that the additional 172 lower-amplitude frequencies listed in Table A.1 also contain physical information, e.g., in terms of even more low-amplitude pulsation modes compared to those considered primarily or some sort of granulation signal which can be interpreted after basic modelling of the 252 dominant ones has been accomplished.

### 3.1.3. Notes on the frequency spectrum

Already upon the first visual inspection of the data we noticed that several features of the light curve and of the periodogram (see Fig. 2) of HD 43317 are similar to those of the other hybrid SPB/ $\beta$  Cep CoRoT star HD 50230 (Degroote et al. 2010a, 2012). HD 43317 is a single relatively fast rotator with a projected rotational velocity of over  $100 \text{ km s}^{-1}$  while this quantity is below  $10 \text{ km s}^{-1}$  for the primary of the binary HD 50230.

As for HD 50230, we ascribe the lower frequencies (below  $2 \text{ d}^{-1}$ ) as due to gravity modes, but in the case of HD 43317 most of the power is distributed over a smaller number of peaks. Compared to HD 50230, we find more frequencies in the range between  $2 \text{ d}^{-1}$  and  $8 \text{ d}^{-1}$ . The typical relative amplitudes of these low-order modes with respect to those of the  $g$  modes are higher ( $\sim 30\%$ ) than in the case of HD 50230 ( $\sim 7\%$ ). Furthermore, these low-order mode frequencies seem to be members of multiplet structures, distributed over peak groups where the density of peaks is higher than in neighbouring regions, except for the very strong and stable isolated peak at  $\sim 4.33 \text{ d}^{-1}$ , which resembles the one at  $\sim 4.92 \text{ d}^{-1}$  in the power spectrum of HD 50230. Given the similar fundamental parameters and the common features of the two power spectra, we expect that these isolated peaks have the same physical origin.

The observed frequencies in a rotating star are related to the pulsational frequency in the co-rotating frame by the expression

$$f = |f' - m f_{\text{rot}}|,$$

where  $f'$  is the frequency in the co-rotating frame and  $f_{\text{rot}}$  is the rotational frequency of the star. For a direct comparison to theoretical predictions, the observed frequency spectrum would need to be converted to the co-rotating frame, but this is not possible without knowing the azimuthal order of the modes. For fast rotators, the difference between the frequency values in the two reference frames can be substantial, and the observed frequencies will spread over a wider range in the periodogram. This might partly explain the excess in number and power of the modes we see above  $2 \text{ d}^{-1}$  compared to HD 50230.

Our frequency analysis method focused on the detection of stable modes with long lifetimes as expected for the dominant modes in this type of star (e.g., Aerts et al. 2010). The highest amplitude closely spaced peaks in the periodogram of HD 43317 indeed cause a typical beating pattern in the short-time Fourier transformation (STFT) (see Fig. 3). These frequencies and their amplitude are stable as prewhitening some of them removes the interference pattern and leaves clear horizontal structures for the remaining ones in the STFT (even in case of the seemingly complicated pattern visible on the upper right image in Fig. 3).

## 4. HARPS spectroscopy

### 4.1. Observations and reduction

In the framework of ground-based preparatory and follow-up observations for the CoRoT space mission, high-resolution and high S/N spectra were taken with the HARPS (Mayor et al. 2003) instrument, in the EGG mode ( $R \approx 80\,000$ ). We refer to Table 2 for a summary of the spectroscopic observations taken simultaneously with the photometric observations.

For a trustworthy abundance analysis (see Sect. 4.2) and for a study of line profile variations (see Sect. 4.3), the normalisation of the spectra is at the same time a crucial and far from trivial step to which we paid special attention. After order-merging,

**Table 2.** Logbook of the spectroscopic observations of HD 43317 obtained during December 2009 – grouped by observing runs.

Instrument	$N$	HJD begin	HJD end	$\langle SNR \rangle$	SNR-range	$T_{\text{exp}}$	$R$
HARPS	132	2 455 174.57665	2 455 183.87419	248	[153, 313]	[240, 600]	80 000
HARPS	59	2 455 191.56933	2 455 195.84863	249	[186, 291]	[250, 500]	80 000

**Notes.** For each observing run, the instrument, the number of spectra  $N$ , the HJD of mid-exposure, the average S/N ratio (calculated as the average S/N in the line free regions of [4490 Å–4505 Å, 4953 Å–4968 Å, 6035 Å–6050 Å, 6738 Å–6753 Å]), the range of SNR values, the typical exposure times (in seconds), and the resolving power of the spectrograph are given.

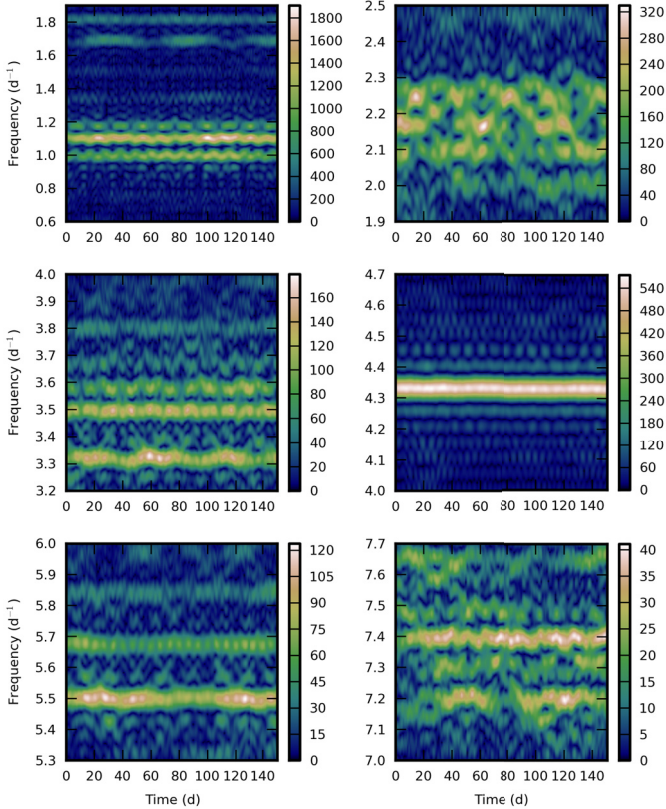


**Fig. 3.** Short-time Fourier transformations of selected regions of the power spectrum (window width of 20 d, colours denote amplitude in ppm). All signal outside these regions was removed before the calculation. Although closely spaced peaks might introduce complicated beating patterns (*upper right*), frequencies appear through the whole light curve.

taking into account the S/N in the overlapping ranges and correcting for the slightly different flux-levels of the overlapping orders (see Fig. 4), we performed a half-automated, two step normalisation of each spectrum. First, after all spectra were brought to the same flux level by dividing them with their median intensity, we defined a master function (using the first spectrum) with cubic splines which were fitted through some tens of points at fixed wavelengths, where the continuum was known to be free of spectral lines. Then we used this function to clean all spectra from large-scale artificial features, e.g., waves in the continuum left there by unsatisfactory flat-fielding. The careful selection of these nodal points enabled us to construct a function which does not distort the shape (and especially the wings) of the Balmer lines. To correct for small scale effects, and a remaining global trend of instrumental origin, we carried out a second normalisation using more nodal points, which were connected by linear functions in this phase. The wavelengths of these points were the same for all spectra, but the normalising function was

constructed for each of them based on the local flux levels, instead of applying a master function again. Using linear functions at this step enabled us to leave the shape of wide features – like the Balmer wings – untouched (by placing only one nodal point at the blue and red end of such regions), but still make small-scale corrections (by using a denser nodal point distribution where it was needed). The described process is much faster, less subjective, and provides better stability than a one-by-one manual normalisation. Furthermore, it can easily be applied to SB1 binaries (or SB2 systems after spectral disentangling), by applying the RV-shifts before normalisation, this way placing the nodal points always at the same position in the zero velocity frame. We found no sign of binarity for HD 43317, so this correction was not necessary.

#### 4.2. Abundance analysis

After normalisation we used different methods to determine the fundamental parameters and abundances from the average normalised spectrum (see Fig. 4).

For a first quick estimate, we carried out a full grid search with four free parameters ( $T_{\text{eff}}$ ,  $\log g$ ,  $v \sin i$ , and the metallicity  $Z$ ), using the precalculated BSTAR2006 grid (Lanz & Hubeny 2007) and the average HARPS spectrum. Chi-square ( $\chi^2$ ) values were calculated using selected regions of H I, He I, Si II, Si III, C II, O II, Mg II, Fe II, S II, and Ne I lines. The results given by the minima of polynomial functions fitted to the  $\chi^2$  values, are listed in Table 3. We did not perform extensive error calculations at this stage, thus the listed errors represent the resolution of the grid. This method suggests Solar metallicity, but note that metallicity can only be changed by scaling to the Solar values – and not element by element – using this grid.

##### 4.2.1. Spectral synthesis

We carried out an LTE-based spectrum analysis, using the range of [4060 Å–5780 Å] of the average spectrum. We used the LLmodels code (Shulyak et al. 2004) in its most recent parallel version to compute the atmosphere models and the SynthV code (Tsymbal 1996) to compute the synthetic spectra. The atmosphere models were computed on a grid in  $T_{\text{eff}}$ ,  $\log g$ , and metallicity with the microturbulence  $\xi_t$  kept fixed to the standard value of  $2 \text{ km s}^{-1}$ .

In a first step, we computed synthetic spectra on a grid in  $T_{\text{eff}}$ ,  $\log g$ ,  $[M/H]$ ,  $\xi_t$ , and  $v \sin i$  based on a precalculated library of atmosphere models. Metallicity in this case means that the abundances of all metals (chemical elements heavier than He) were scaled by the same factor compared to the Solar composition.

In the second step, we adjusted the abundances of single chemical elements with the SynthV code by using the atmosphere models computed for the fixed, optimum metallicity derived in the first step and by taking the abundance table corresponding to that metallicity as an initial guess. The abundances

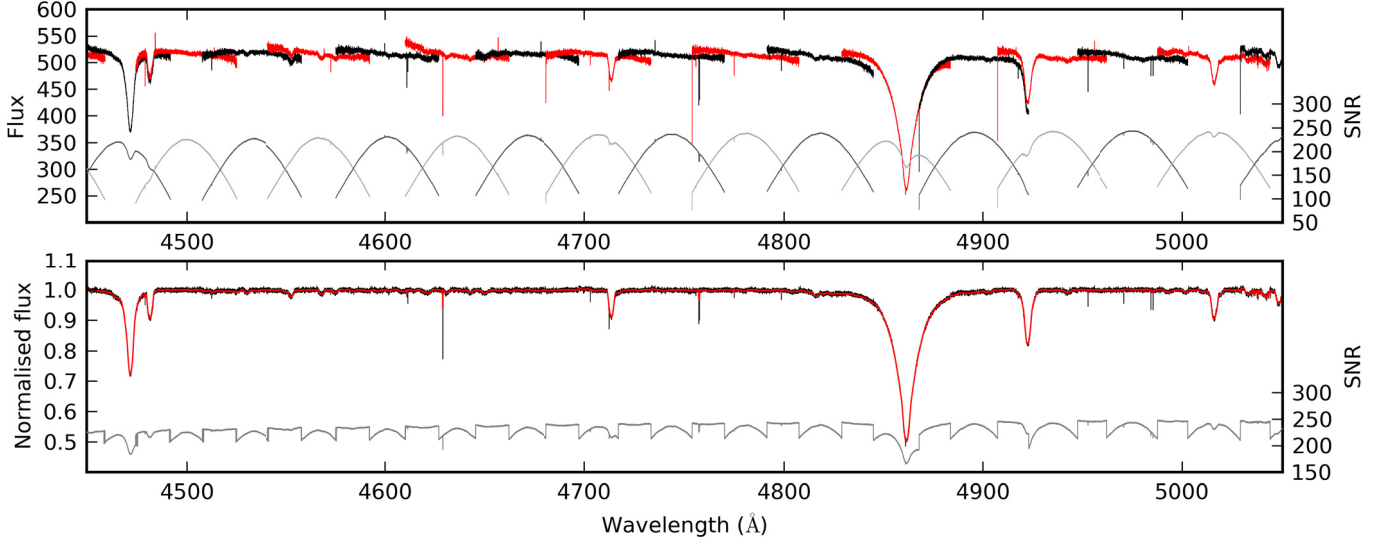


**Fig. 4.** *Upper panel:* a typical raw HARPS spectrum (consecutive orders plotted with a different colour for better visibility). *Lower panel:* the same spectrum after order merging, normalisation, and the removal of cosmics which were not removed by the standard pipeline (with the average of all spectra also plotted in red). Signal-to-noise levels are also plotted order-by-order and for the merged spectrum. Detailed explanation of the process can be found in the text.

**Table 3.** Fundamental stellar parameters derived from spectroscopy using different methods, model atmospheres, and line formation codes.

Method	Quick look grid-search	Spectral synthesis	Equivalent widths
Atmosphere	NLTE	LTE	LTE
Line formation	NLTE	LTE	NLTE
$T_{\text{eff}}$ (K)	$17\,350 \pm 1000$	$16\,800 \pm 100$	$17\,750 \pm 250$
$\log g$ (cgs)	$4.0 \pm 0.25$	$3.9 \pm 0.1$	$4.1 \pm 0.1$
$v \sin i$ (km s $^{-1}$ )	$108 \pm 10$	$106 \pm 4$	$115 \pm 9$
$\xi_t$ (km s $^{-1}$ )	2 (preset)	$3.35 \pm 0.80$	$3 \pm 3$ (preset)
Spectral type <sup>a</sup>		B4 V-IV	B3.5 V

**Notes.** <sup>(a)</sup> Spectral type had been determined based on  $T_{\text{eff}}$  and  $\log g$  values by using an interpolation in the tables given by Schmidt-Kaler (1982).

**Table 4.** Abundances derived from different methods based on different model atmospheres and line formation codes compared to Solar values and a cosmic abundance standard.

Element	LTE /LTE	LTE /NLTE (n lines)	GS98 <sup>a</sup>	AGS05 <sup>b</sup>	AGSS09 <sup>c</sup>	PNB08 <sup>d</sup>
He	$11.13 \pm 0.20$	$10.78 \pm 0.27$ (8)	$10.93 \pm 0.004$	$10.93 \pm 0.01$	$10.93 \pm 0.01$	$10.98 \pm 0.02$
C	$8.14 \pm 0.20$	$8.00 \pm 0.28$ (2)	$8.52 \pm 0.06$	$8.39 \pm 0.05$	$8.43 \pm 0.05$	$8.32 \pm 0.03$
N		$7.66 \pm 0.28$ (2)	$7.92 \pm 0.06$	$7.78 \pm 0.06$	$7.83 \pm 0.05$	$7.76 \pm 0.05$
O	$8.11 \pm 0.20$	$8.77 \pm 0.24$ (2)	$8.83 \pm 0.06$	$8.66 \pm 0.05$	$8.69 \pm 0.05$	$8.76 \pm 0.03$
Ne		$7.99 \pm 0.12$ (5)	$8.08 \pm 0.06$	$7.84 \pm 0.06$	$7.93 \pm 0.10$	$8.08 \pm 0.03$
Mg	$7.18 \pm 0.20$	$7.23 \pm 0.39$ (1)	$7.58 \pm 0.05$	$7.53 \pm 0.09$	$7.60 \pm 0.04$	$7.56 \pm 0.05$
Si	$6.86 \pm 0.20$	$7.45 \pm 0.26$ (4)	$7.55 \pm 0.05$	$7.51 \pm 0.04$	$7.51 \pm 0.03$	$7.50 \pm 0.02$
S	$6.74 \pm 0.20$		$7.33 \pm 0.11$	$7.14 \pm 0.05$	$7.12 \pm 0.03$	
Fe	$6.80 \pm 0.20$		$7.50 \pm 0.05$	$7.45 \pm 0.05$	$7.50 \pm 0.04$	$7.44 \pm 0.04$

**Notes.** All abundances are given in units of  $\log(\text{El}/\text{H}) + 12/\text{atoms per } 10^6 \text{ nuclei}$ . <sup>(a)</sup> Grevesse & Sauval (1998); <sup>(b)</sup> Asplund et al. (2005); <sup>(c)</sup> Asplund et al. (2009); <sup>(d)</sup> Przybilla et al. (2008).

were iterated simultaneously with other parameters like  $T_{\text{eff}}$ ,  $\log g$ ,  $\xi_t$ , and  $v \sin i$  until the minimum in  $\chi^2$  has been found.

In the final step, we did a fine-tuning of the fundamental parameters ( $T_{\text{eff}}$ ,  $\log g$ ,  $\xi_t$ ,  $v \sin i$ ) by using the table with derived abundances and the atmosphere models computed for the metallicity determined in the first step. A more detailed description as well as tests of the method can be found in Lehmann et al. (2011).

Atmospheric parameters and individual abundances determined in this way are listed in Tables 3 and 4, along with results from other methods. Since the abundances of all metals (in col-

umn labelled with LTE/LTE in Table 4) agree with the derived metallicity of  $[\text{M}/\text{H}] = -0.38 \pm 0.10^1$  within the error bars, we conclude that there is no need to recompute the atmosphere models assuming individual chemical composition and, consequently, there is no need to do re-adjustment of the fundamental parameters.

<sup>1</sup> Relative to the Solar metallicity given by Asplund et al. (2005).

#### 4.2.2. Equivalent widths and line ratios

To check the dependence of our results on the input physics and different methods, we also carried out a detailed abundance study based on an extensive grid of synthetic spectra based on the latest versions of the NLTE line formation codes DETAIL and SURFACE originally developed by Butler (1984) and Giddings (1981), along with plane-parallel, fully line-blanketed LTE Kurucz atmospheric models (Kurucz 1993). It was shown by Nieva & Przybilla (2007) that this hybrid approach is adequate for B stars on the main sequence. For further details on the grid and the iterative method of analysis along with the error calculations, we refer to Morel et al. (2006), and discuss only the key points of our case below.

The projected rotational velocity over  $\sim 100 \text{ km s}^{-1}$  causes such a large line broadening that is it hard to find lines without significant blending, which is needed to measure equivalent widths (EWs) precisely. The first task was the construction of a proper line list. The error values in Table 4 mainly result from the small number of lines and the sensitivity of the abundances to changes in the effective temperature. We also had to fix the value of microturbulence at  $3 \pm 3 \text{ km s}^{-1}$ , which is a typical value for main sequence B3 stars (see, e.g., Nieva & Przybilla 2010), because we did not have enough lines to determine it from requiring independence between the abundances and the line strengths. Microturbulence is generally found to be higher only in evolved objects (see, e.g., Cantiello et al. 2009).

For spectral type B3, we observe only the two ionisation stages Si II and Si III, which we used to determine the effective temperature. Here we were not only restricted by the need of unblended lines, but also by the fact that some lines are not properly modelled (Simón-Díaz 2010). We fitted the wings of the H $\alpha$ , H $\beta$ , H $\gamma$ , and H $\delta$  lines to fix the  $\log g$  value (see Table 3).

To be consistent, we used the same set of lines (8 He I and 16 metal lines) as in the abundance analysis to measure the projected rotational velocity,  $v \sin i$ , with the Fourier-method described by Simón-Díaz et al. (2006). We calculated the  $v \sin i$  for all lines separately, and estimated the error as the standard deviation of these values (see Table 3).

#### 4.2.3. Discussion of results from different methods

Compared to the underabundance of metals we found from the spectral synthesis in Sect. 4.2.1, the second method (see column labelled with LTE/NLTE in Table 4) leads to abundances in agreement with the Solar values within the error bars (except – although the errors are large – for carbon). The results for helium are less clear but the Solar values are still within the error bars for both analyses. The low metallicity from the LTE/LTE method would not lead to excitation (see, e.g., the instability strips calculated for different metallicities in Miglio et al. 2007), while the Solar abundances from the LTE/NLTE method agree well with similar results found for other B stars (Morel 2009) or the proposed cosmic abundance standard derived from B stars in the Solar neighbourhood by Przybilla et al. (2008). The differences in the resulting abundances and in the systematic uncertainty of 1000 K in the effective temperature illustrate that the LTE treatment for line formation is incorrect in this temperature range. Przybilla et al. (2011) warns against the blind use of the BSTAR2006 grid, as oversimplification in the model atom descriptions might cause problems for some of the complex ions/elements. This should not be an issue here, as only a few weak lines of such elements were taken into account.

**Table 5.** Frequencies derived from the Fourier analysis of the line moments.

	Frequency ( $\text{d}^{-1}$ )	
	He I at 6678 Å	Mg II at 4481 Å
$\langle v \rangle$	2.23	
	1.10	1.35
		1.10
		1.69
$\langle v^2 \rangle$	2.23	
	4.33	4.33
$\langle v^3 \rangle$	2.23	
	1.10	1.10
	1.69	1.69

**Notes.** The errors of the frequencies are  $1/T_{\text{spectr.}} \approx 0.05 \text{ d}^{-1}$ .

Given the above, we consider the parameters listed in the last column of Table 3 (and the corresponding abundances from Table 4) as the best estimates we can get. As the error in effective temperature is an internal – and probably unrealistically small – value, we prefer to adopt a typical error of  $\pm 1000 \text{ K}$  instead. Using the distance measurement from van Leeuwen and the available colour excess values (see Sect. 2.1) the estimated  $M_V = -1.40 \pm 0.51$  is fully consistent – through the spectral class of B3.5 V which is based on the derived fundamental parameters – with our results (based on the tables provided by Straizys & Kuriliene 1981).

#### 4.3. Study of line profile variations

Pulsations result in radial velocity changes and variations in spectral line profiles. Depending on the degree  $\ell$  and azimuthal order  $m$ , modes leave characteristic patterns in the spectroscopic data, which can be used for mode identification if we are able to decipher them. In order to achieve this, we use the pixel-by-pixel method to detect the pulsation frequencies from the variation in the line profiles and use the Fourier-parameter fit (FPF) method (Zima 2006) to identify the modes, as well as the line profiles' moments (Briquet & Aerts 2003). We have investigated our spectroscopic data using both methods, but the broad lines imply the pixel-by-pixel method to be best suited.

As discussed by Aerts et al. (2010, Chaps. 4 and 6), it is best to perform spectroscopic mode identification from one unblended deep line, whose width is dominated by thermal broadening and not affected by pressure broadening. For the case of HD 43317, the He I line at 6678 Å and the Mg II line at 4481 Å fulfill these requirements best. We thus treat them first. Further on, we discuss the variability behaviour of other spectral lines.

##### 4.3.1. The line moments

We calculated the first three moments ( $\langle v \rangle$ ,  $\langle v^2 \rangle$ , and  $\langle v^3 \rangle$ ) for the selected helium and magnesium lines and computed their discrete Fourier-transform function (DFT) using the FAMIAS software package (Zima 2008). The results are listed in Table 5. All frequencies in Table 5 match significant peaks found in the CoRoT dataset (see Table A.1). Given that the frequency precision from the spectroscopy is an order of magnitude lower (Rayleigh frequency of  $1/T_{\text{spectr.}} \approx 0.05 \text{ d}^{-1}$ ), the match is not always unambiguous.

The frequency content for the two spectral lines is not completely overlapping. There is a frequency which can be only

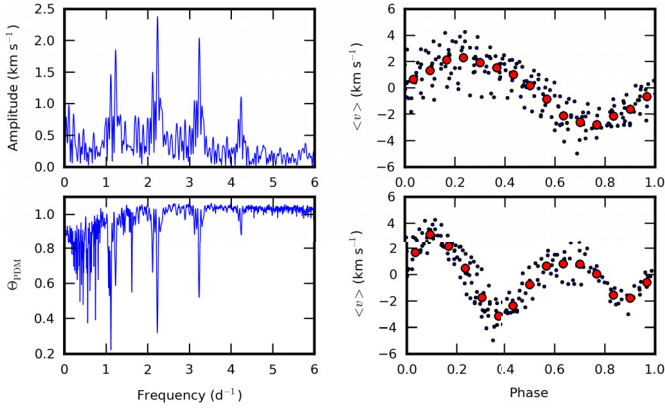


**Fig. 5.** Upper left: scargle periodogram of  $\langle v \rangle$  of the He I line at 6678 Å with the highest peak at  $\sim 2.23 \text{ d}^{-1}$ . Upper right: phase-plot of  $\langle v \rangle$  according to the frequency  $f_m = 2.228748 \text{ d}^{-1}$ . The small symbols are observations, while the larger red circles are phase-binned averages. Lower left:  $\Theta_{\text{PDM}}$ -statistics of  $\langle v \rangle$ , showing the deepest minimum at  $f_m/2$ . Lower right: phase-plot of  $\langle v \rangle$  according to the frequency  $f_m/2$ .

found in the moments of the He I line at 6678 Å ( $\sim 2.23 \text{ d}^{-1}$ ), and there is a frequency which can be found in the Mg II line at 4481 Å alone ( $\sim 1.35 \text{ d}^{-1}$ ).

The highest peak in the DFT of the first moment of the He line is  $\sim 2.23 \text{ d}^{-1}$  and its phase-plot shows a sine pattern with moderate scatter. However, the phase dispersion minimisation (PDM, see [Stellingwerf 1978](#)) technique suggests that the true frequency is half the value found from the DFT, which clearly leads to a lower scatter in the phase diagram (Fig. 5). The EW of the He I line at 6678 Å shows the same behaviour as the first moment (with a small phase shift between the two). The Mg line does not show such double-wave nature.

#### 4.3.2. Variability in other selected lines

Following [Aerts et al. \(2010\)](#) we investigated if we could increase the significance of the line profile variability in a global sense, by applying the Least Square Deconvolution technique (LSD, [Donati et al. 1997](#); [Kennelly et al. 1998](#)). In order to do so, we started from the set of unblended lines selected in Sect. 4.2. Such methods only deliver useful and better results than individual lines if their variability has the same amplitude, phase, and intrinsic broadening for all the profiles considered in the merging. Given their strong Stark broadening, H lines are excluded for such tests while He lines must be treated separately from the metal lines. Small blends will lead to uncertainties, especially when the number of lines used for the calculation is low, and must be avoided.

We calculated two sets of LSD profiles, one using only helium lines, and another one based on metal lines, and compared their behaviour to the one of the He I line at 6678 Å and of the Mg II line at 4481 Å. In case of the He I lines, the LSD profiles are slightly asymmetric as the individual lines have small blends in their wings. Even though the line depths are the same, and the signal-to-noise of the LSD profiles is far higher than the one of the single He I line at 6678 Å, its variability amplitude is only half that of the individual line. In the case of the metal lines, the LSD profiles are shallower, and even though their signal-to-noise levels are higher, their variability signal is again only half that of the individual Mg II line at 4481 Å.

**Table 6.** Frequencies derived from the pixel-by-pixel analysis of the line profiles.

Frequency ( $\text{d}^{-1}$ )		$l$	$m$	$i$ ( $^\circ$ )
He I at 6678 Å	Mg II at 4481 Å			
2.23				
1.36	1.35	3	3	29
4.45				
3.58	3.58	8, 7	0	34
4.33	4.33	2 ( $\geq 2$ )	2 ( $\geq 0$ )	23 (20–40)
6.68				
1.11?				
	2.76?			

**Notes.** The errors of the frequencies are  $1/T_{\text{spectr.}} \approx 0.05 \text{ d}^{-1}$ . Values with a question mark are non-secure frequencies. For the discussion of mode identification see Sect. 4.3.4.

The derived frequencies for both sets are identical to those found in the individual lines and we do not find any additional ones. This shows that, also globally in the spectrum, the He I lines behave differently than the metal lines, except for the Si II lines (e.g., at 5640 Å) and the Ne I lines (e.g., at 6096 Å, 6143 Å, 6267 Å, 6402 Å, and 6507 Å) which show similar behaviour to the He I lines. The rest of the metal lines with clear line-profile variability, e.g., C II at 4267 Å, Si II at 5056 Å, 6347 Å, 6371 Å, Si III at 4553 Å, and 4568 Å, behave in a similar manner to the selected Mg II line, but add to the complexity in the LSD due to small blends and various levels of thermal broadening.

We conclude that we could not improve the results of the frequency detection and mode identification from the LSD technique, which is not really surprising in the case of hot stars given their limited number of spectral lines.

#### 4.3.3. Pixel-by-pixel variations

The frequencies found with the pixel-by-pixel method are listed in Table 6. Just as in case of the line moments, all frequencies can be matched to significant peaks found in the CoRoT photometry. For both spectral lines, the dominant frequency matches the one found in the line moments. Phase-plots of the line profiles according to these frequencies are shown in Fig. 6.

All frequencies derived from the Mg II line at 4481 Å are also found in the pixel-by-pixel variations of the He I line at 6678 Å. The additional frequencies in the He line are  $\sim 2.23 \text{ d}^{-1}$ ,  $\sim 4.45 \text{ d}^{-1}$ , and  $\sim 6.68 \text{ d}^{-1}$ . The frequency  $\sim 1.11 \text{ d}^{-1}$  is also present in the residuals, but it does not meet our significance criterion of having a S/N level above 4. However, all the frequencies which can only be found in the variations of the He line are even harmonics of  $\sim 1.11 \text{ d}^{-1}$ .

#### 4.3.4. Interpretation and discussion

We interpret the spectroscopic variability as due to rotation combined with pulsations. The harmonics detected across the He line, as well as in its EW and first moment, point towards a spotted or at least inhomogeneous surface configuration. The fact that such a harmonic structure is not detected in the Mg line points out that we are dealing with temperature and/or chemical variations, to which the He (and Ne) lines are more sensitive than the Mg line.

The spectroscopic variability leads to the conclusion that  $\sim 1.11 \text{ d}^{-1}$  is the rotation frequency of the star. Indeed, the

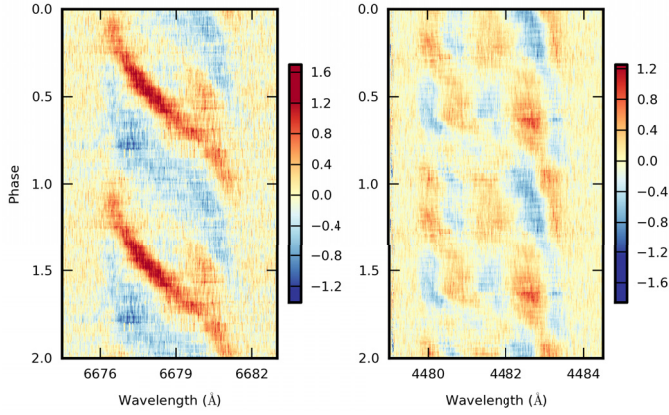


**Fig. 6.** A colour scale representation of the residual spectral lines with respect to the average line for the selected He and Mg line of HD 43317. The phase corresponds to the dominant period found through the pixel-by-pixel method, colours denote deviations from the average profile in percentage. For better visibility of the patterns, two cycles are shown, and we have applied an S/N-weighted sliding boxcar smoothing with a bin width of 0.05 and a step size of 0.005 cycles. *Left:* phase-plot for the He I line at 6678 Å using the dominant frequency of  $2.228748 \text{ d}^{-1}$ . *Right:* phase-plot for the Mg II line at 4481 Å using the dominant frequency of  $1.354276 \text{ d}^{-1}$ .

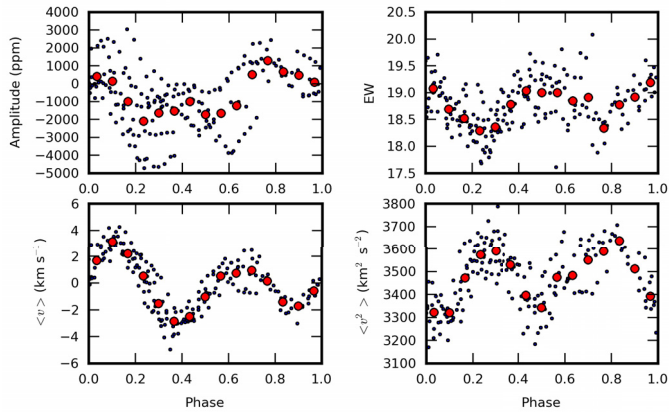


**Fig. 7.** Phase-plots using the rotation frequency  $f_{\text{rot}} = 1.114997 \text{ d}^{-1}$ . *Upper left:* the subset of CoRoT data averaged over the HARPS integration times when simultaneous spectroscopy is available. The cycle-to-cycle variations are due to the dominant pulsation modes. *Upper right:* the EW; *lower panels:*  $\langle v \rangle$  and  $\langle v^2 \rangle$  of the He I line at 6678 Å. The small symbols are observations, while the larger red circles are phase-binned averages.

variations in the moments of the He I line at 6678 Å are best explained in terms of rotational modulation and the resulting double bump in the phase-plots (Fig. 7) was already detected and interpreted as such before in other B stars as well. The moments of HD 43317 have the same characteristics as those of the B6 star HD 105382 (see Briquet et al. 2001, 2004) while they are atypical for pulsations (see Aerts et al. 1992; Clarke 2003).

Furthermore, the autocorrelation function of the CoRoT light curve gives the strongest peak around a period of  $\sim 0.9 \text{ d}$  (Fig. 8) and not half this period. The rotation frequency is not the highest peak in the Scargle periodogram of the CoRoT light curve ( $1.100615 \text{ d}^{-1}$ ), but does occur among the largest-amplitude signals at  $f_{\text{rot}} = 1.114997 \text{ d}^{-1}$ . This is indeed a perfect match with  $f_{\text{m}}/2$  where  $f_{\text{m}} = 2.228748 \text{ d}^{-1}$  is adopted from the Fourier-analysis of  $\langle v \rangle$  of the He I line at 6678 Å. The frequency  $f_{\text{rot}}$  is

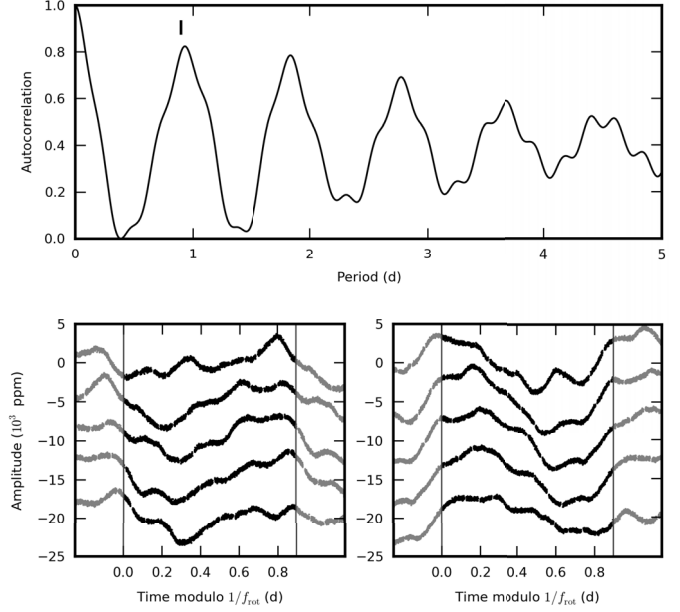


**Fig. 8.** *Upper panel:* autocorrelation function of the CoRoT light curve. The period corresponding to the proposed  $f_{\text{rot}}$  rotational frequency is marked with a thick vertical line. The same scaling is used as for Fig. 9. *Lower panels:* sample consecutive cuts of the CoRoT light curve according to a period of  $1/f_{\text{rot}}$  showing strong similarities. For better visibility the previous and following cuts are also plotted in grey, while the consecutive orders are shifted downwards by 5000 ppm.

found as a significant peak very close to the dominant pulsation frequency even when the light curve is cut into two halves.

Further evidence supporting  $f_{\text{rot}}$  to correspond with the rotation frequency comes from the fact that a series of harmonics for  $f_{\text{rot}}$  was detected up to  $7f_{\text{rot}}$  in the CoRoT light curve (these are marked in Table A.1) while no harmonics were found for the numerous other frequencies. The amplitude of the harmonics of  $f_{\text{rot}}$  follows a decreasing trend, with the even harmonics having higher amplitude than the odd ones above  $2f_{\text{rot}}$ . The systematic effect that the observed frequencies differ slightly from the exact harmonics was also found in the case of the B0.5 IV star HD 51756 (Pápics et al. 2011), where it was explained in terms of differential rotation. The simultaneous occurrence of rotational modulation and pulsations was also found in the case of the CoRoT B2.5 V target HD 48977 (Thoul et al. 2012), but the frequency resolution is less for that star.

From models along the evolutionary tracks with input physics in Briquet et al. (2011), we consider a typical value of the radius of  $R = 3.8 R_{\odot}$  for  $T_{\text{eff}} = 17\,000 \text{ K}$ ,  $\log g = 4.0$  (cgs), and a metallicity of  $Z = 0.014$ . This results in  $v_{\text{eq}} \approx 214 \text{ km s}^{-1}$ . This, combined with the measured projected rotational velocity  $v \sin i \approx 110 \text{ km s}^{-1}$ , gives an inclination angle  $i \approx 30^{\circ}$ . A corresponding typical mass in the models is  $M = 5.4 M_{\odot}$  and leads to a critical velocity of  $v_{\text{cr}} \approx 425 \text{ km s}^{-1}$  (in the definition of Cranmer & Owocki 1995). These radius and mass values, and the deduced critical velocity, are averages for the considered model grid and are in agreement with the ones in the calibration tables of Straizys & Kuriliene (1981) for the spectral type B3.5 V which we derived in Sect. 4.2. Thus, the star is rotating at  $\sim 50\%$  of its critical velocity. Since we do not detect any signs of emission in the spectrum, as expected for a star rotating at the break-up limit and thus losing material, it is unlikely that  $f_{\text{m}}$  is the rotation frequency.

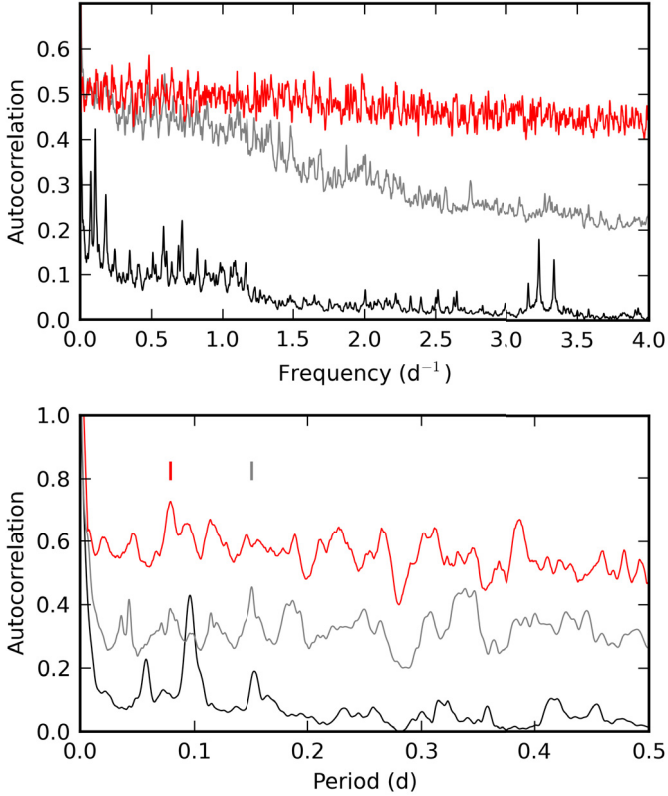


**Fig. 9.** *Upper panel:* autocorrelation function of the full power spectrum in frequency space. The autocorrelation of the original power spectrum is plotted in black, the one of the power spectrum after prewhitening the 6 strongest peaks is plotted in grey, and then one of the 252 significant frequencies given an artificial power while all others given zero power in red. *Lower panel:* autocorrelation functions of the power spectrum between  $0.5 \text{ d}^{-1}$  and  $2 \text{ d}^{-1}$ , converted into period space (colours have the same meaning). Candidate spacings are marked with a thick vertical line using a colour according to the corresponding function.

We restricted the estimated inclination value for the mode identification ( $i \in [20^\circ, 40^\circ]$ ) using the FPF method in FAMIAS, which takes into account rotations effects due to the Coriolis force in the modelling of the pulsations (for the practical details, we refer to Zima 2006, 2008). We applied it to the three common modes which were found in the pixel-by-pixel analysis of both data sets in Sect. 4.3.3. The results are shown in Table 6. For the frequency at  $\sim 1.36 \text{ d}^{-1}$ , we performed the analysis on both selected spectral lines, with the same result. For the two other frequencies, we used only the Mg line, as the influence from the harmonics of the rotational frequency was too high in the He line, causing the residual signal to be much weaker in that case. Based on both the  $\chi^2$  values and the visual check of the amplitude and phase fits, we are confident in the mode identification of  $\ell = m = 3$  for the peak at  $\sim 1.36 \text{ d}^{-1}$ , while for the two other peaks our level of confidence is lower, especially in case of the frequency at  $\sim 4.33 \text{ d}^{-1}$ . Although the best fit is achieved with  $\ell = m = 2$ , the quality of the fit itself is not very convincing, especially given the large spread in  $\ell$  and  $m$  within a small range in  $\chi^2$ .

We have to note that all the available mode identification methods, including those implemented in FAMIAS, are based on a perturbative treatment of the rotation of the star. This is doubtful in the case of gravito-inertial modes (Ballot et al. 2010), i.e., modes for which  $f < 2f_{\text{rot}}$ . All the frequencies in Table A.1 with

value below  $2.23 \text{ d}^{-1}$  are in that regime, in particular the dominant one at  $\sim 1.36 \text{ d}^{-1}$ . In that sense, also the identification of that dominant mode must be treated as preliminary.

Given that the Coriolis force changes the propagation cavities for gravito-inertial modes compared to those of g modes with  $f > 2f_{\text{rot}}$ , it might be that the dominant mode's excitation, and the one of all the modes in that regime, were affected by the rotation of the star. This could be an explanation why the relative strength of the g modes in this star with respect to the p modes, is different than in the case of the slow rotator HD 50230.

## 5. Search for characteristic spacings

Although fitting individual frequency values is generally thought to deliver good constraints on the models of massive stars (see, e.g., Auserloos et al. 2004), it relies on the assumption that there is no offset between observed and computed oscillation frequencies in the case of stars with a radiative envelope. In order to be less dependent of this assumption, it is worthwhile to search for useful seismic diagnostics to model, such as frequency and/or period spacings, as well as rotational splittings.

The autocorrelation function of the power spectrum of the CoRoT light curve is shown in Fig. 9. The few strong peaks each correspond with the frequency difference between two of the dominant modes. The autocorrelation function computed after the six strongest modes have been removed, no longer shows prominent peaks and has similar behaviour as the one we obtained from the spectrum containing the 252 significant frequencies when all these modes were given the same artificial power and all other frequencies more than half the Rayleigh frequency away from the 252 under consideration were placed at value zero.

Although the autocorrelation functions (see Fig. 9) do not result in apparent spacing values, we find not only triplets, but also series of more components. We considered all candidate spacings in the data, starting from pairs to longer series, using the set of 252 accepted frequencies, for a tolerance set to the Rayleigh frequency. After having found candidates, we confronted them with the autocorrelation functions.

It is hard to exclude rotational splitting as interpretation of a spacing without knowing the  $\ell$  and  $m$  values. In fact, rotational splittings of HD 43317 can easily be asymmetric due to the relatively high rotational frequency, and we may have missed rotational multiplets due to this reason with our criteria.

To find appropriate candidates for frequency and period chains, we looked for series having a high average amplitude, a relatively small scatter (standard deviation) of amplitudes, and containing many peaks. The longest series we found in this way is one with ten consecutive peaks (see Fig. 10), having an average period spacing of 6339 s (0.07337 d). This value is physically meaningful for B3 V stars (e.g., Aerts & Dupret 2011) and is of the same order as the spacing value found for the slow rotator HD 50230 (9418 s, Degroote et al. 2010a). As in that paper, we also find small deviations from the exact spacing value, with an average absolute deviation of 197 s (0.00228 d). In addition to this longest series of consecutive peaks, we find another one with seven components, whose peaks do not overlap with the previous series and having an average period spacing of 6380 s (0.07385 d), with a deviation of 430 s (0.00498 d). This series is also indicated in Fig. 10.

The dominant spectroscopic mode is not a member of the series found. This is as expected, given that it has an  $\ell = 3$  while we expect the two detected long series of peaks from the photometry to correspond with  $\ell = 1$  or 2 modes having the same

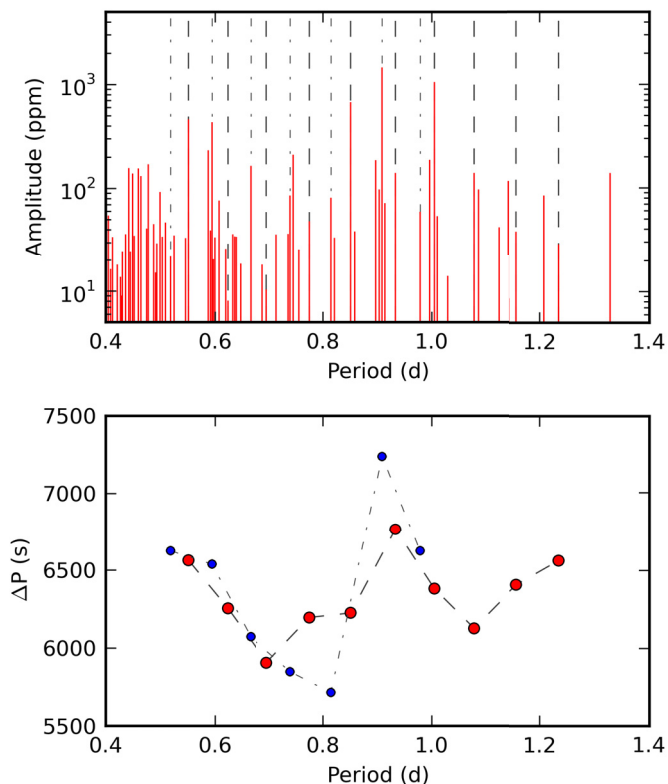


**Fig. 10.** *Upper panel:* the period spectrum of the CoRoT light curve of HD 43317 (red solid lines), with the locations of the members of the two longest series with almost constant period spacing in grey dashed, and dash-dotted lines. *Lower panel:* the deviations from the average period spacings are indicated through line connections between the members of the two series.

azimuthal order within the series. In fact, given that the found period spacing of the two series is about the same suggests that we are dealing with one  $\ell$ -value and different  $m$ -values. It is not a critical issue that we are unable to convert these frequencies to a co-rotating frame without the secure knowledge of their azimuthal orders, as from a modelling point of view the frequency spacings of the series are of main importance, and the transformation between the two reference frames does not affect these values.

Additional shorter sequences of frequencies also occur, but they contain less consecutive peaks and are thus more prone to randomness. They could be suitable for interpretation once the main sequences of frequencies can be well identified and fitted by model frequencies.

## 6. Conclusions

Our observational seismic study of the fast rotator HD 43317 by means of CoRoT space photometry and high-precision HARPS spectroscopy led to its classification as a new bright hybrid  $\beta$ Cep/SPB star. The star rotates at about half its critical velocity and shows clear evidence of rotational modulation in addition to its pulsational variability in both the photometry and the spectroscopy. The list of B-type stars with a detected mixture of rotational and pulsational variability with similar frequencies and amplitudes is growing and occurs across all effective temperatures of this spectral type (e.g., Uytterhoeven et al. 2005; Degroote et al. 2011; Thoul et al. 2012). This is not surprising

given the co-existence of chemically peculiar Bp and SPB stars in the same part of the HR diagram (e.g., Briquet et al. 2007).

With the CoRoT target HD 43317, we deliver the second pulsating B star for which almost constant period spacings of its high-order g modes have been detected. As shown by Degroote et al. (2010a), this offers the potential to tune the details of the conditions, in particular the level and nature of mixing, near the stellar core of such stars. In the case of HD 50230, this was done ignoring the effects of the slow rotation of the star on the behaviour of its g modes, a valid assumption for that star given its equatorial rotation velocity below  $10 \text{ km s}^{-1}$ . HD 43317 has a factor ten higher rotational frequency and we are thus in a more complex situation. Interpretation of the detected period spacings near 6300 s and their small deviation in terms of the input physics of stellar models, as it was done in the case of the slow rotator HD 50230 (9418 s, Degroote et al. 2010a), first requires secure identification of the wavenumbers ( $\ell, m$ ) of the modes corresponding to the frequency peaks indicated in Fig. 10. In particular, we must unravel if all the peaks in one series correspond with one value of the azimuthal order  $m$ , and, if so, with which one. Given that we were unable to detect those frequencies in HARPS spectroscopy, such an identification must come from predictions of oscillation modes from theoretical stellar models. In computing such pulsation predictions, it must be taken into account that many of the detected gravity modes of HD 43317 fall in the regime of the gravito-inertial modes, whose propagation cavities are modified by the Coriolis force. This is in particular the case for all the 17 frequencies occurring in the two series with the constant period spacing we found. The description of such modes requires full computations with respect to the rotation of the star, rather than approximations based on a perturbative approach.

*Acknowledgements.* The research leading to these results has received funding from the European Research Council under the European Community's Seventh Framework Programme (FP7/2007–2013)/ERC grant agreement No. 227224 (PROSPERITY), as well as from the Belgian Science Policy Office (Belspo, C90309: CoRoT Data Exploitation). E.P. and M.R. acknowledge financial support from the PRIN-INAF 2010 *Asteroseismology: looking inside the stars with space- and ground-based observations*. T.M. acknowledges financial support from Belspo for contract PRODEX-GAIA DPAC. M.H. acknowledges support by the Austrian Fonds zur Förderung der wissenschaftlichen Forschung (FWF, project P22691-N16).

## References

- Abt, H. A., Levato, H., & Grosso, M. 2002, *ApJ*, 573, 359
- Aerts, C., de Pauw, M., & Waelkens, C. 1992, *A&A*, 266, 294
- Aerts, C., Thoul, A., Daszyńska, J., et al. 2003, *Science*, 300, 1926
- Aerts, C., Christensen-Dalsgaard, J., & Kurtz, D. W. 2010, *Asteroseismology* (Heidelberg: Springer)
- Aerts, C., Briquet, M., Degroote, P., Thoul, A., & van Hoolst, T. 2011, *A&A*, 534, A98
- Asplund, M., Grevesse, N., & Sauval, A. J. 2005, in *Cosmic Abundances as Records of Stellar Evolution and Nucleosynthesis*, ed. T. G. Barnes III, & F. N. Bash, ASP Conf. Ser., San Francisco, 336, 25
- Asplund, M., Grevesse, N., Sauval, A. J., & Scott, P. 2009, *ARA&A*, 47, 481
- Ausseloss, M., Scuflaire, R., Thoul, A., & Aerts, C. 2004, *MNRAS*, 355, 352
- Auvergne, M., Bodin, P., Boisnard, L., et al. 2009, *A&A*, 506, 411
- Ballot, J., Lignières, F., Reese, D. R., & Rieutord, M. 2010, *A&A*, 518, A30
- Blackwell, D. E., Shallis, M. J., & Selby, M. J. 1979, *MNRAS*, 188, 847
- Blomme, R., Mahy, L., Catala, C., et al. 2011, *A&A*, 533, A4
- Bonneau, M. 1967, *J. Observ.*, 50, 237
- Breger, M., Stich, J., Garrido, R., et al. 1993, *A&A*, 271, 482
- Briquet, M., & Aerts, C. 2003, *A&A*, 398, 687
- Briquet, M., De Cat, P., Aerts, C., & Scuflaire, R. 2001, *A&A*, 380, 177
- Briquet, M., Aerts, C., Lüftinger, T., et al. 2004, *A&A*, 413, 273
- Briquet, M., Hubrig, S., De Cat, P., et al. 2007, *A&A*, 466, 269
- Briquet, M., Aerts, C., Baglin, A., et al. 2011, *A&A*, 527, A112
- Butler, K. 1984, Ph.D. Thesis, University of London, UK

- Cantiello, M., Langer, N., Brott, I., et al. 2009, *A&A*, 499, 279
- Castelli, F., & Kurucz, R. L. 2003, in *Modelling of Stellar Atmospheres*, ed. N. Piskunov, W. W. Weiss, & D. F. Gray, IAU Symp., 210, 20P
- Chapellier, E., Rodríguez, E., Auvergne, M., et al. 2011, *A&A*, 525, A23
- Clarke, D. 2003, *A&A*, 407, 1029
- Cranmer, S. R., & Owocki, S. P. 1995, *ApJ*, 440, 308
- Crawford, D. L., Barnes, J. V., Hill, G., & Perry, C. L. 1971, *AJ*, 76, 1048
- Cucchiari, A., Jaschek, M., Jaschek, C., & Macau-Hercot, D. 1976, *A&AS*, 26, 241
- Cutri, R. M., Skrutskie, M. F., van Dyk, S., et al. 2003, *2MASS All Sky Catalog of point sources*
- Cutri, R. M., Wright, E. L., Conrow, T., et al. 2011, *Explanatory Supplement to the WISE Preliminary Data Release Products*, Tech. Rep.
- Degroote, P., Briquet, M., Catala, C., et al. 2009, *A&A*, 506, 111
- Degroote, P., Aerts, C., Baglin, A., et al. 2010a, *Nature*, 464, 259
- Degroote, P., Briquet, M., Auvergne, M., et al. 2010b, *A&A*, 519, A38
- Degroote, P., Acke, B., Samadi, R., et al. 2011, *A&A*, 536, A82
- Degroote, P., Aerts, C., Michel, E., et al. 2012, *A&A*, in press, DOI: 10.1051/0004-6361/201118548
- Donati, J., Semel, M., Carter, B. D., Rees, D. E., & Collier Cameron, A. 1997, *MNRAS*, 291, 658
- Giddings, J. R. 1981, Ph.D. Thesis, University of London, UK
- Gilliland, R. L., Brown, T. M., Christensen-Dalsgaard, J., et al. 2010, *PASP*, 122, 131
- Grevesse, N., & Sauval, A. J. 1998, *Space Sci. Rev.*, 85, 161
- Guetter, H. H. 1968, *PASP*, 80, 197
- Gutiérrez-Soto, J., Floquet, M., Samadi, R., et al. 2009, *A&A*, 506, 133
- Hauck, B., & Mermilliod, M. 1998, *A&AS*, 129, 431
- Heiles, C. 2000, *AJ*, 119, 923
- Høg, E., Fabricius, C., Makarov, V. V., et al. 2000, *A&A*, 355, L27
- Hohle, M. M., Neuhäuser, R., & Schutz, B. F. 2010, *Astron. Nachr.*, 331, 349
- Houk, N., & Swift, C. 1999, *Michigan catalogue of two-dimensional spectral types for the HD Stars*, ed. N. Houk, & C. Swift, 5
- Kawaler, S. D., Sekii, T., & Gough, D. 1999, *ApJ*, 516, 349
- Kennelly, E. J., Brown, T. M., Kotak, R., et al. 1998, *ApJ*, 495, 440
- Kurucz, R. 1993, *ATLAS9 Stellar Atmosphere Programs and 2 km s<sup>-1</sup> grid*, Kurucz CD-ROM No. 13, Cambridge, Mass.: Smithsonian Astrophysical Observatory, 13
- Kuschnig, R., Weiss, W. W., Gruber, R., Bely, P. Y., & Jenkner, H. 1997, *A&A*, 328, 544
- Lanz, T., & Hubeny, I. 2007, *ApJS*, 169, 83
- Lefever, K., Puls, J., Morel, T., et al. 2010, *A&A*, 515, A74
- Lehmann, H., Tkachenko, A., Semaan, T., et al. 2011, *A&A*, 526, A124
- Lesh, J. R. 1968, *ApJS*, 17, 371
- Mayor, M., Pepe, F., Queloz, D., et al. 2003, *The Messenger*, 114, 20
- Mermilliod, J. C. 1986, *Bulletin d'Information du Centre de Données Stellaires*, 31, 185
- Miglio, A., Montalbán, J., & Dupret, M. 2007, *CoAst*, 151, 48
- Morel, T. 2009, *Communications in Asteroseismology*, 158, 122
- Morel, T., Butler, K., Aerts, C., Neiner, C., & Briquet, M. 2006, *A&A*, 457, 651
- Morgan, H. R. 1956, *AJ*, 61, 90
- Murakami, H., Baba, H., Barthel, P., et al. 2007, *PASJ*, 59, 369
- Nieva, M. F., & Przybilla, N. 2007, *A&A*, 467, 295
- Nieva, M.-F., & Przybilla, N. 2010, in *Hot and Cool: Bridging Gaps in Massive Star Evolution*, ed. C. Leitherer, P. Bennett, P. Morris, & J. van Loon, ASP Conf. Ser., San Francisco, 425, 146
- Pápics, P. I., Briquet, M., Auvergne, M., et al. 2011, *A&A*, 528, A123
- Poretti, E., Michel, E., Garrido, R., et al. 2009, *A&A*, 506, 85
- Przybilla, N., Nieva, M., & Butler, K. 2008, *ApJ*, 688, L103
- Przybilla, N., Nieva, M.-F., & Butler, K. 2011, *J. Phys. Conf. Ser.*, 328, 012015
- Rufener, F. 1988, *Catalogue of stars measured in the Geneva Observatory photometric system*, 4
- Rufener, F., & Nicolet, B. 1988, *A&A*, 206, 357
- Savage, B. D., Massa, D., Meade, M., & Wesselius, P. R. 1985, *ApJS*, 59, 397
- Schmidt-Kaler, T. 1982, *Landolt-Börnstein*, ed. K. Schaifers, & H. H. Vogt, Vol. 2b (Springer-Verlag, Berlin)
- Shull, J. M., & van Steenberg, M. E. 1985, *ApJ*, 294, 599
- Shulyak, D., Tsymbal, V., Ryabchikova, T., Stütz, C., & Weiss, W. W. 2004, *A&A*, 428, 993
- Simón-Díaz, S. 2010, *A&A*, 510, A22
- Simón-Díaz, S., Herrero, A., Esteban, C., & Najarro, F. 2006, *A&A*, 448, 351
- Stellingwerf, R. F. 1978, *ApJ*, 224, 953
- Straizys, V., & Kuriliene, G. 1981, *Ap&SS*, 80, 353
- Thompson, G. I., Nandy, K., Jamar, C., et al. 1978, *Catalogue of stellar ultraviolet fluxes*, A compilation of absolute stellar fluxes measured by the Sky Survey Telescope (S2/68) aboard the ESRO satellite TD-1, (NASA/STI)
- Thoul, A., Degroote, P., Catala, C., et al. 2012, *A&A*, submitted
- Tsymbal, V. 1996, in *M.A.S.S., Model Atmospheres and Spectrum Synthesis*, ed. S. J. Adelman, F. Kupka, & W. W. Weiss, ASP Conf. Ser., San Francisco, 108, 198
- Uytterhoeven, K., Briquet, M., Aerts, C., et al. 2005, *A&A*, 432, 955
- van Leeuwen, F. 2007, *A&A*, 474, 653
- Weber, S. V., Henry, R. C., & Carruthers, G. R. 1971, *ApJ*, 166, 543
- Wesselius, P. R., van Duinen, R. J., Aalders, J. W. G., & Kester, D. 1980, *A&A*, 85, 221
- Wesselius, P. R., van Duinen, R. J., de Jonge, A. R. W., et al. 1982, *A&AS*, 49, 427
- Westin, T. N. G. 1985, *A&AS*, 60, 99
- Wolff, S. C., Edwards, S., & Preston, G. W. 1982, *ApJ*, 252, 322
- Wright, C. O., Egan, M. P., Kraemer, K. E., & Price, S. D. 2003, *AJ*, 125, 359
- Wright, E. L., Eisenhardt, P. R. M., Mainzer, A. K., et al. 2010, *AJ*, 140, 1868
- Zima, W. 2006, *A&A*, 455, 227
- Zima, W. 2008, *CoAst*, 155, 17